

# Breaking a superfluid harmonic dam: Observation and theory of rarefaction flow, Riemann invariants and sonic horizon dynamics

Shashwat Sharan,<sup>1</sup> Judith Gonzalez Sorribes,<sup>2</sup> Patrick Sprenger,<sup>1</sup>  
Mark A. Hoefer,<sup>3</sup> P. Engels,<sup>4</sup> Boaz Ilan,<sup>1,\*</sup> and M. E. Mossman<sup>2,4,†</sup>

<sup>1</sup>*Department of Applied Mathematics, University of California, Merced, Merced, CA, USA 95343*

<sup>2</sup>*Department of Physics and Biophysics, University of San Diego, San Diego, CA, USA 92110*

<sup>3</sup>*Department of Applied Mathematics, University of Colorado, Boulder, CO, USA*

<sup>4</sup>*Department of Physics and Astronomy, Washington State University, Pullman, WA, USA 99164*

Dilute-gas Bose-Einstein condensates are a prime testbed for the study of superfluid hydrodynamics. In a channel geometry, these systems are known to host prototypical hydrodynamic effects such as shocks, rarefaction waves and solitons, forming a bridge between classical and quantum dynamics. Here, we present a combined experimental and theoretical study of the dry-bed dam-break problem in a channel geometry, a hallmark problem of nonlinear dynamics. Our setup extends the canonical setting by adding harmonic confinement, or an effective bathymetry, along the channel, further enhancing the richness of dynamics. We obtain an analytical solution of the 1D Gross-Pitaevskii (GP) equation for the harmonic dam-break problem that provides further insight. Experimentally, we characterize the flow by measuring its Riemann invariant coordinates and find good agreement with computations of the 3D GP equation as well as with the analytical solution. Our experimental observation of a sonic horizon, and the prediction of collisions between such horizons at longer times, offer an intriguing perspective for further studies.

Hydrodynamics spans a vast range of scales and systems ranging from rivers and oceans to neutron stars and the early universe. Central to the study of nonlinear wave dynamics are Riemann problems, which represent idealized initial-value problems characterized by an initial discontinuity separating two different states of a fluid. Riemann problems have been extensively studied due to their ability to succinctly capture essential features of wave evolution and interactions, making them fundamental benchmarks in hydrodynamic theory [1–6]. Key to the analysis of Riemann problems are Riemann invariants (RIs), specific combinations of fundamental hydrodynamic variables, such as fluid density and flow velocity, that remain constant along characteristic curves [7, 8]. This property simplifies the analysis of wave propagation and provides a powerful tool for characterizing the dynamics. A prominent example within this context is the dam-break problem, which models the evolution of two fluid states separated by a barrier. Following the instantaneous removal of this barrier, the fluid evolves into distinct wave structures, typically including rarefaction waves (RWs) and shock waves. A special subclass of this scenario is the vacuum dam-break problem, characterized by a vanishing density on one side of the initial discontinuity. In this configuration, the fluid expands freely into the vacuum region, giving rise to a *simple* RW that is described by two distinct RIs, one of which remains constant throughout the wave expansion.

The analytical simplicity and coherent wave structures arising from dam-break flows in classical hydrodynamics have motivated their application and study across various physical contexts, such as nonlinear optics [9–11], magnetohydrodynamics [12–15], magneto-gas-dynamics [16], and dilute-gas Bose-Einstein condensates (BECs) [17–19]. The common underlying nonlinear wave dynamics shared by these diverse systems facilitate the transfer of analytical insights and methods from classical hydrodynamics to these other domains. However,

real-world systems typically deviate from idealized conditions assumed in Riemann problems due to perturbations such as external potentials, dissipative effects, or variations in initial conditions. These perturbations disrupt the simple RI structure, and lead to more complex flow dynamics. Understanding these deviations is essential for determining how realistic conditions affect nonlinear wave behavior, motivating further studies of such complex systems.

In this Letter, we undertake precisely such an investigation, extending the classic dam-break problem into the superfluid regime which includes a weak harmonic trap. This type of confinement is a common feature in channel-like BEC experimental setups, where it introduces an effective bathymetry to the problem. Analogous to the role bathymetry plays in shoaling waves or tsunamis, the harmonic trap here modifies fluid dynamics, influencing the structure and evolution of the RIs that characterize the complex flow. To experimentally measure RIs within our flow, we introduce a method to determine the local flow speeds and the speed of sound. The observed values agree with the 3D numerics and analytical solutions of the system. For the harmonic rarefaction flows studied here, we show that one of the RIs is approximately conserved for short times, consistent with the idealized case, while at longer times, new superfluid dynamics arise. Complementing the experiments, we present a complete analytical characterization of the RIs, which accounts for the harmonic trap and reveals new features within the rarefaction flow. We identify the behavior of sonic horizons [20–24] within harmonic rarefaction flows and present an investigation of the formation of such horizons in a BEC. Sonic horizons have attracted significant interest in multiple settings, including water [25], ion rings [26], and BECs [27–31]. For our system, numerical simulations also demonstrate a collision between two sonic horizons at longer evolution times, opening the way for further investigations.

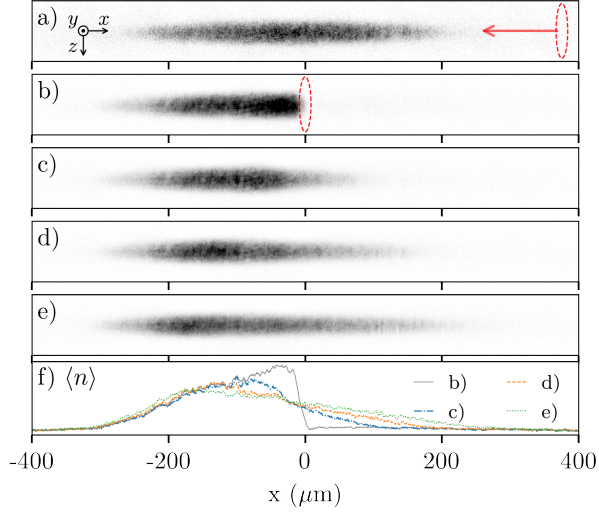


FIG. 1. Evolution of a rarefaction fan. a) A repulsive optical barrier or dam (represented by the red dashed oval) is slowly swept  $523(1) \mu\text{m}$  from the right to the center of the BEC in 2 s. b) The dam is removed at  $t = 0$  and atoms are allowed to flow into the  $x > 0$  region of the trap, e.g. for c)  $t = 20$  ms, d)  $t = 40$  ms, and e)  $t = 60$  ms. f) Integrated cross sections of the density are provided for panels b)-e), where the canonical parabolic profile appears at short times. Data has been averaged over five experimental runs of the same parameters.

To provide context for the discussion of the superfluid dam break, we begin with a brief discussion of the experimental setup. A BEC, composed of  $\mathcal{N} \approx 1.1 \times 10^6$   $^{87}\text{Rb}$  atoms in the  $|F, m_F\rangle = |1, -1\rangle$  state, is held in an optical dipole trap with trap frequencies  $\{\omega_x, \omega_y, \omega_z\} = 2\pi \times \{2.45, 243, 251\}$  Hz, yielding an initial chemical potential of  $\mu \approx 104$  nK. To create an effective dam, a blue-detuned laser ( $\lambda = 660$  nm) propagating in the  $z$ -direction is employed that can be shifted along the  $x$ -direction via a tunable galvanometer. With Gaussian waists  $\{s_x, s_y\} = \{9.6(1), 56.5(4)\} \mu\text{m}$ , the potential produced by this laser in the  $y$ -direction extends well beyond the tight radial confinement of the cloud. The peak height of this potential is  $U_d \approx 408$  nK, such that the atoms do not tunnel through the barrier when traveling at the speeds considered in this work.

To generate a controlled rarefaction flow, we use this dam potential to create a dry-bed dam-breaking scenario. This procedure is explained and depicted in the experimental images of Fig. 1a–e. After an adiabatic sweep of the potential from the outside (Fig. 1a), the BEC is in a Thomas-Fermi (TF) ground state, occupying the left half of the harmonic trap (Fig. 1b). When the dam potential is suddenly removed, the BEC rarefies into the previously unoccupied region where  $x > 0$  as shown in Fig. 1c–e. In the absence of the trap, this is predicted to generate a dry-bed rarefaction wave, with parabolic density and linear flow velocity profiles. The observed density profiles are highlighted in Fig. 1f. The rarefaction flow in our experimental setting extends over hundreds of microns, providing ample space for the propagation and investigation of hydrodynamic features.

We characterize the rarefaction flow in our system by determining the RIs. To facilitate this analysis, we model the flow using an effective 1D GP equation [32],

$$i\hbar\partial_t\psi = \left( -\frac{\hbar^2}{2m}\partial_x^2 + \frac{1}{2}m\omega_x^2x^2 + g_{1d}|\psi|^2 \right)\psi, \quad (1)$$

where  $\hbar$  is the reduced Planck constant,  $m$  is the atomic mass of  $^{87}\text{Rb}$ , and  $g_{1d}$  is the effective 1D interatomic coupling constant. This reduction is valid when the transverse confinement is significantly stronger than the axial confinement, and the system can be treated as effectively 1D. In this model,  $g_{1d} \approx 0.238$  (see End Matter), and  $\psi$  is normalized such that  $\int |\psi|^2 dx = \mathcal{N}$  where  $\mathcal{N}$  is the total number of atoms  $\mathcal{N}$  in the BEC.

The 1D GP equation (1) can be reformulated in terms of hydrodynamic variables using the Madelung transformation,  $\psi = \sqrt{n}e^{im\phi/\hbar}$ , where  $n = |\psi|^2$  denotes the local atom density and  $\phi$  is the velocity potential, so that the flow velocity in the  $x$  direction is  $u = \partial_x\phi$ . Substituting this transformation into Eq. (1) yields the system

$$\partial_t n + \partial_x(nu) = 0, \quad (2a)$$

$$\partial_t(nu) + \partial_x\left(nu^2 + \frac{g_{1d}n^2}{2m} - \frac{\hbar^2 n}{4m^2}\partial_x^2(\log n)\right) = -n\omega_x^2x. \quad (2b)$$

Equation (2a) describes local mass conservation while Eq. (2b) describes momentum balance, which includes hydrodynamic pressure ( $\propto g_{1d}$ ), quantum pressure ( $\propto \hbar^2$ ), and the harmonic trap ( $\propto \omega_x^2$ ). Since our system is in the TF regime, the quantum pressure is negligible compared to the hydrodynamic pressure (see End Matter). Ignoring this term allows the system to be diagonalized in terms of the RI variables,

$$r_{\pm} = \frac{u}{2} \pm c_s, \quad c_s = \sqrt{\frac{g_{1d}n}{m}}, \quad (3)$$

where  $c_s$  is the local speed of sound. We refer to  $r_+$  as the fast RI and  $r_-$  as the slow RI because their corresponding characteristic speeds,  $v_{\pm} = u \pm c_s$ , satisfy  $v_+ > v_-$ , making  $r_+$  associated with faster wave propagation. The diagonalization results in the following system of two coupled equations for  $r_{\pm}$ ,

$$\partial_t r_{\pm} + \frac{1}{2}(3r_{\pm} + r_{\mp})\partial_x r_{\pm} = -\frac{1}{2}\omega_x^2x. \quad (4)$$

In the absence of the trap ( $\omega_x = 0$ ), this diagonal system admits the self-similar solution

$$r_+(x, t) = s_0, \quad r_-(x, t) = -\frac{s_0}{3} + \frac{2x}{3t}, \quad (5)$$

which describes the expanding region of a *simple* RW solution, where  $s_0$  is the speed of sound at the initial peak density. The solution (5) is defined within  $x_l(t) < x < x_r(t)$ , where the left and right edges are given by  $x_l(t) = -s_0t$  and  $x_r(t) = 2s_0t$ , respectively [33]. The right edge, here, corresponds to the vacuum point of the RW. This solution is classified as *simple* because one of the RIs is conserved. Specifically, the fast RI is constant, while the slow RI exhibits self-similar behavior in the variable  $x/t$  within the expansion region.

In the presence of a spatially varying external potential, simple wave solutions do not exist, and both RIs are expected to show spatiotemporal variations. As an important contribution of this work, we present an exact solution of Eq. (4) in the presence of a harmonic trap:

$$r_+(x, t) = \frac{s_0 \cos\left(\frac{\omega_x t}{4}\right) - \frac{\omega_x x}{2} \sin\left(\frac{3\omega_x t}{4}\right)}{\cos\left(\frac{3\omega_x t}{4}\right)}, \quad (6a)$$

$$r_-(x, t) = \frac{-s_0 \sin\left(\frac{\omega_x t}{4}\right) + \frac{\omega_x x}{2} \cos\left(\frac{3\omega_x t}{4}\right)}{\sin\left(\frac{3\omega_x t}{4}\right)}. \quad (6b)$$

This solution (6) reduces to the simple RW solution (5) in the vanishing potential limit  $\omega_x \rightarrow 0$ . A small  $\omega_x t$  expansion reveals that  $r_+(x, t) \sim s_0 + \left(\frac{s_0}{4} - \frac{3x}{8t}\right)(\omega_x t)^2$ , indicating that  $r_+$  remains approximately conserved at short times but varies for longer times. Similarly,  $r_-(x, t) \sim -\left(\frac{s_0}{3} - \frac{2x}{3t}\right) - \left(\frac{s_0}{36} + \frac{x}{8t}\right)(\omega_x t)^2$ , which shows that  $r_-$  is approximately self-similar in  $x/t$  at short times but deviates from self-similarity at longer times.

Using Eq. (6), the expressions for the local speed of sound and the flow velocity can be obtained as  $c_s = \frac{1}{2}(r_+ - r_-)$  and  $u = r_+ + r_-$ , respectively, yielding

$$c_s(x, t) = \frac{\omega_x}{2} \csc\left(\frac{3\omega_x t}{2}\right)(x_r(t) - x), \quad (7a)$$

$$u(x, t) = \frac{2s_0 + \omega_x x \cos\left(\frac{3\omega_x t}{2}\right) \csc\left(\frac{\omega_x t}{2}\right)}{1 + 2 \cos(\omega_x t)}, \quad (7b)$$

where the vacuum point  $x_r(t) = \frac{2s_0}{\omega_x} \sin(\omega_x t)$  defines the right edge of the rarefaction flow. Remarkably, this solution has vanishing quantum pressure and thus satisfies the full 1D hydrodynamic system (2) and, consequently, the 1D GP equation (1) with a harmonic trap.

The exact solution given by Eq. (7) predicts a linear spatial profile for the speed of sound within the rarefaction flow region. Numerical simulations, however, reveal that at longer times the true speed of sound profile deviates significantly from linearity away from the vacuum point. At the vacuum point, the exact solution remains accurate, acting as a tangent line to the true numerically observed profile. To obtain an explicit solution that is accurate across the entire rarefaction region, we employ a matched expansion method. The rarefaction region is  $x_l(t) < x < x_r(t)$ , where we find that the left edge is well-approximated by (see End Matter)

$$x_l(t) = -\frac{\sqrt{2}s_0}{\omega_x} \sin\left(\frac{\omega_x t}{\sqrt{2}}\right). \quad (8)$$

We assume that the speed of sound and flow velocity take a quadratic spatial form with time-dependent coefficients

$$c_{s,\text{match}}(x, t) = c_0(t) + c_1(t)x + c_2(t)x^2, \quad (9a)$$

$$u_{\text{match}}(x, t) = u_0(t) + u_1(t)x + u_2(t)x^2. \quad (9b)$$

The coefficients  $c_j(t)$  and  $u_j(t)$  for  $j \in \{0, 1, 2\}$  are determined by requiring that (i) the right-edge connects smoothly with the solution in Eq. (7), and (ii) the left-edge is continuous with the

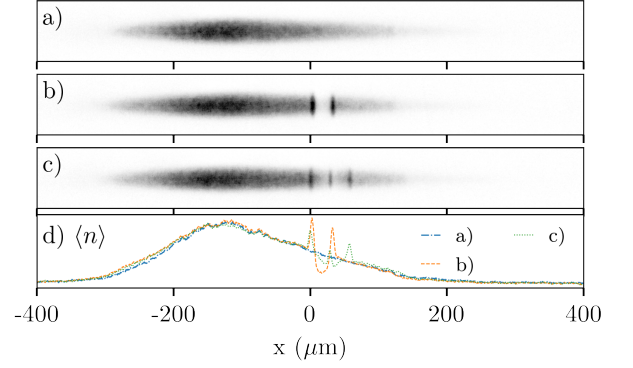


FIG. 2. Barrier pulse procedure. a) At  $t = 40$  ms rarefaction wave flows to the right. b) The barrier is shifted to a position, here at  $x = 21 \mu\text{m}$ , pulsed on for  $500 \mu\text{s}$ , and then imaged. c) After the barrier is pulsed on, excitations are allowed to evolve for  $5$  ms, then imaged again. d) Integrated cross sections with arbitrary units of the experimental process. All images taken in a  $5$  ms time-of-flight. Images are averaged over  $10$  experimental runs with the same parameters.

initial TF profile (see End Matter). Using this matched solution, the RIs across the entire rarefaction flow are computed using Eq. (3) and are discussed in the context of the experimental results below.

The central role played by the RIs motivates the development of an experimental method to robustly measure these quantities. Here, we describe such a method using a barrier-pulse procedure. For this, first a rarefaction flow is generated, as described in Fig. 1. We then pulse the barrier potential on for  $0.5$  ms at a new position  $x_c$ . This generates two sharp, high-density excitations on either side of the barrier. Relative to the rarefaction flow, these excitations travel outwards at approximately the speed of sound [17, 34–36]. This experimental procedure is demonstrated in Fig. 2.

To determine the RIs, we first characterize the local flow velocity and speed of sound in the system by measuring the positions of the two high-density excitations at  $0$  and  $5$  ms after the barrier pulse. The local background flow velocity is determined by averaging the left- and right-moving velocities of the high-density peaks,  $u_{\text{loc}} = \frac{1}{2}(v_+ + v_-)$ , while the local speed of sound is found by subtracting the local flow velocity from the right-moving velocity,  $c_{s,\text{loc}} = v_+ - u_{\text{loc}} = \frac{1}{2}(v_+ - v_-)$ . From these local hydrodynamic variables, the two measured RIs are computed using Eq. (3). By repeating this procedure for various positions  $x_c$  and times  $t$ , we experimentally determine the spatio-temporal dependence of the RIs.

The experimental and theoretical values of  $r_{\pm}$ , measured at five different rarefaction times ( $t \leq 60$  ms) and at various spatial locations are presented in Fig. 3. To facilitate a direct comparison of datasets corresponding to different times, Fig. 3 reports the values for  $r_{\pm}$  as a function of  $x_c/t$ , where  $x_c$  (the pulse location) is scaled by  $t$  for each data set. When scaled in this way, both fast and slow RIs exhibit approximate universal behaviors in the shaded region of Fig. 3. In particular, for

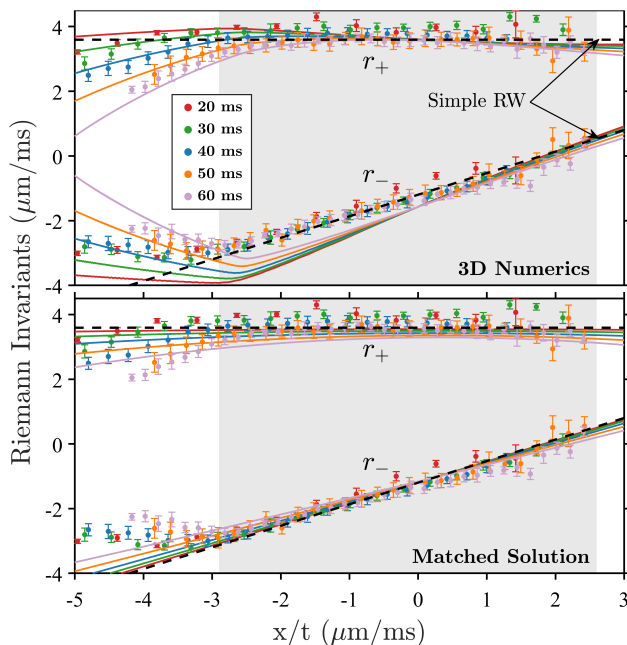


FIG. 3. Measured slow ( $r_-$ ) and fast ( $r_+$ ) RIs along the channel at different rarefaction flow times (data points with error bars, see legend). Measurement errors are determined by the standard deviation of the mean at each probed position. The 3D GP numerical simulations (solid curves, upper panel) and matched solutions from Eq. (9) (solid curves, lower panel) are shown for comparison. The simple RW solution (5) (black dashed line), initially describes  $r_-$ , with the slope decreasing over time due to harmonic confinement, as predicted by the exact solution (6). The initial offset in the slope of the RIs in the 3D numerics can be attributed to the use of integrated density cross-section to compute the RIs. The shaded region denotes the rarefaction flow region where the matched solution is valid and experimental data is available.

short times, a substantial portion of the data collapses closely onto the universal simple RW solution Eq. (5) indicative of self-similar behavior with a characteristic slope of  $2/3$ . At longer times, a clear departure from this self-similar regime is evident as the slope progressively decreases, consistent with predictions from the exact analytical solution (6).

These experimental and analytical results quantitatively describe how the quantum dam-break problem results in a classical RW that, early on, conserves the fast RI,  $r_+$ , and then develops into a more complex harmonic rarefaction flow. To further highlight this complexity, we investigate the existence and dynamics of sonic horizons in rarefaction flows.

While performing this barrier pulse procedure along the BEC, the excitation generated to the left of the barrier – generated against the flow – can move at a velocity exactly opposite to the local flow velocity in the system. This position is shown in Fig. 4 as a red solid curve, in which the computational results are based on solutions of the 3D GP equation. These excitations are unable to move beyond a sonic horizon,  $x_{\text{SH}}$ , realizing an acoustic white hole [23, 37, 39], while excitations generated in the region  $x > x_{\text{SH}}$  travel down the rarefaction wave. For short times ( $t < 100$  ms), as the rarefaction fan evolves,  $x_{\text{SH}}$  initially

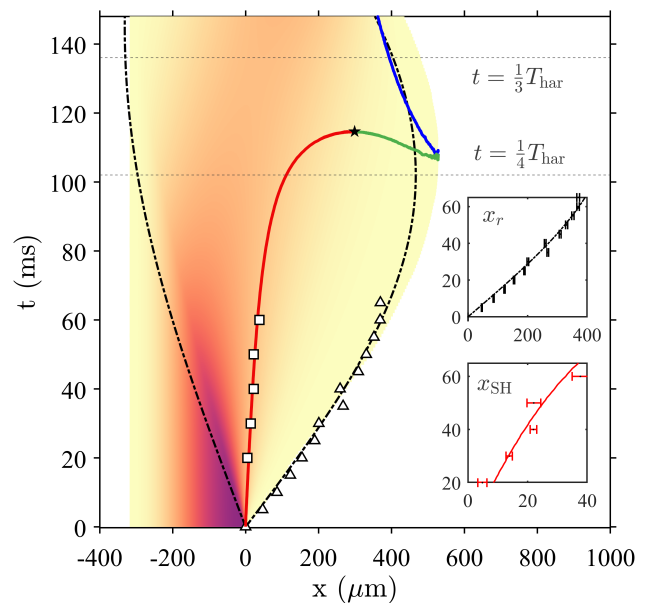


FIG. 4. Spatiotemporal evolution of BEC density. The background shows the integrated cross-sectional density  $\langle n \rangle$  from 3D GP simulations using experimental parameters. Solid curves track sonic horizons: two “fast” horizons (red and green, where  $u_{\text{loc}} - c_{s,\text{loc}} = 0$ ) and one “slow” horizon (blue, where  $u_{\text{loc}} + c_{s,\text{loc}} = 0$ ), with their collision marked by a star. Black dot-dashed curves are 1D predictions for the rarefaction edges from Eqs. (7)-(8). Experimental data for the sonic horizon (squares) and right edge of the rarefaction (triangles) are overlaid. Horizontal dashed lines mark 1D turnaround and gradient catastrophe times. Insets magnify the right edge rarefaction and sonic horizon trajectories for  $t \leq 60$  ms, with measurement errors obtained by averaging data from multiple experimental runs.

accelerates away from  $x = 0$  in the positive direction.

For longer times, we note that the solution Eq. (6) is time-periodic with a period  $2T_{\text{har}}$ , where  $T_{\text{har}} = \frac{2\pi}{\omega_x}$  is the harmonic trap period. The rarefaction flow solution Eq. (7) predicts that the vacuum point of the condensate undergoes a turn-around at  $\frac{1}{4}T_{\text{har}}$ , where it momentarily comes to rest before reversing direction due to the harmonic trap. Notably, this turn-around time coincides with that of the condensate’s center of mass. Following the turn-around, this solution predicts a gradient catastrophe at  $\frac{1}{3}T_{\text{har}}$ , where the density gradient diverges at the vacuum boundary. Furthermore, the solution (7) satisfies the property  $r_+(x, t) = r_-(x, t + T_{\text{har}})$ , implying that after one trap period, the roles of the RIs are interchanged.

The computations shown in Fig. 4 predict the emergence of a second sonic horizon (green curve) at low densities (*i.e.*, at low  $c_{s,\text{loc}}$ ) as the atoms approach the turning point. As the system evolves, these two horizons approach each other and annihilate. A third sonic horizon (blue) also emerges at the turning point in the trap and begins to flow back to the center, albeit more slowly than the second horizon. An experimental verification for these dynamics present an intriguing outlook for future work.

In summary, we have provided a detailed theoretical and experimental analysis of a superfluid dam-break problem. We

presented a robust experimental method for determining RIs in an elongated BEC, as well as theoretical and numerical simulations that are in full agreement with our experiments. In particular, an exact analytical solution describing the evolution of the RIs, and thus density and flow velocity profiles, in the presence of a harmonic trap was presented. An intriguing aspect of the flow field in our study is the dynamics of a sonic horizon that we experimentally determined. Our theory also predicts additional sonic horizons to emerge at later times, one of which annihilates with another horizon.

This work introduces a line of questions for future studies, including long-time rarefaction revival dynamics in a trap, dam-break reflections [40, 41], controlled sonic horizon dynamics [21, 42], and investigations of rarefaction from dams of various shapes [43].

J.G.S. and M.E.M. acknowledge support from the National Science Foundation (NSF) through Grant No. PHY-2137848. M.E.M. additionally acknowledges funding from NSF through Grant No. DMS-1941489 and from the Clare Boothe Luce Professorship Program of the Henry Luce Foundation. P.E. acknowledges support from the NSF through Grant No. PHY-2207588 and from a Boeing Endowed Professorship at WSU. M.A.H. acknowledges support from NSF via Grant No. DMS-2306319. P.E., M.A.H., S.S., P.S., and B.I. would like to thank the Isaac Newton Institute for Mathematical Sciences, Cambridge, for support and hospitality during the programme "Emergent phenomena in nonlinear dispersive waves", where work on this paper was undertaken. This programme was supported by EPSRC grant EP/R014604/1.

*Author Contributions* J.G.S., P.E., and M.E.M. conceived and performed the experiments and data analysis. S.S., P.S., B.I., and M.A.H. performed theoretical calculations and numerical simulations. All authors discussed the results and contributed to the writing of the manuscript.

*Competing Interests* The authors declare no competing interests.

*Materials & Correspondence* Please direct any questions or requests concerning this article to M. Mossman or B. Ilan.

*Code Availability* All relevant code used for numerical studies in this work is available from the corresponding authors upon reasonable request.

*Data Availability* All relevant experimental and numerical data sets in this work will be made available from the corresponding authors upon reasonable request.

---

\* [bilan@ucmerced.edu](mailto:bilan@ucmerced.edu)

† [mmossman@sandiego.edu](mailto:mmossman@sandiego.edu)

- [1] J. Miles and D. Henderson, Parametrically forced surface waves, *Annual Review of Fluid Mechanics* **22**, 143 (1990).
- [2] F. Bonnefoy, A. Tikan, F. Copie, P. Suret, G. Ducrozet, G. Prabhudesai, G. Michel, A. Cazaubiel, E. Falcon, G. El, and S. Randoux, From modulational instability to focusing dam breaks in water waves, *Physical Review Fluids* **5**, 034802 (2020).
- [3] H. von Häfen, C. Krautwald, H. Bihs, and N. Goseberg, Dam-break waves' hydrodynamics on composite bathymetry, *Frontiers in Built Environment* **8**, 10.3389/fbuil.2022.877378 (2022).
- [4] F. Garoosi, A. Nicole Mellado-Cusica, M. Shademani, and A. Shakibaenia, Experimental and numerical investigations of dam break flow over dry and wet beds, *International Journal of Mechanical Sciences* **215**, 106946 (2022).
- [5] H. O. Marangoz, T. Anilan, and S. Karasu, Investigating the non-linear effects of breach parameters on a dam break study, *Water Resources Management* **38**, 1773 (2024).
- [6] D. K. Muchiri, J. N. Hewett, M. Sellier, M. Moyers-Gonzalez, and J. Monnier, Numerical simulations of dam-break flows of viscoplastic fluids via shallow water equations, *Theoretical and Computational Fluid Dynamics* **38**, 557 (2024).
- [7] J. Smoller and J. Smoller, Riemann invariants, entropy, and uniqueness, *Shock Waves and Reaction-Diffusion Equations*, 391 (1983).
- [8] G. B. Whitham, *Linear and nonlinear waves* (John Wiley & Sons, 2011).
- [9] G. Xu, M. Conforti, A. Kudlinski, A. Mussot, and S. Trillo, Dispersive dam-break flow of a photon fluid, *Physical Review Letters* **118**, 254101 (2017).
- [10] F. Audo, B. Kibler, J. Fatome, and C. Finot, Experimental observation of the emergence of Peregrine-like events in focusing dam break flows, *Optics Letters* **43**, 2864 (2018).
- [11] L. Dieli, D. Pierangeli, E. DelRe, and C. Conti, Observation of two-dimensional dam break flow and a gaseous phase of solitons in a photon fluid, *Physical Review Letters* **133**, 183801 (2024).
- [12] C. C. Wu, Magnetohydrodynamic Riemann problem and the structure of the magnetic reconnection layer, *Journal of Geophysical Research: Space Physics* **100**, 5579 (1995).
- [13] B. Giacomazzo and L. Rezzolla, The exact solution of the Riemann problem in relativistic magnetohydrodynamics, *Journal of Fluid Mechanics* **562**, 223 (2006).
- [14] K. Takahashi and S. Yamada, Exact Riemann solver for ideal magnetohydrodynamics that can handle all types of intermediate shocks and switch-on/off waves, *Journal of Plasma Physics* **80**, 255 (2013).
- [15] T. Minoshima and T. Miyoshi, A low-dissipation HLLD approximate Riemann solver for a very wide range of Mach numbers, *Journal of Computational Physics* **446**, 110639 (2021).
- [16] R. Singh and L. Singh, Solution of the Riemann problem in magnetogasdynamics, *International Journal of Non-Linear Mechanics* **67**, 326 (2014).
- [17] J. J. Chang, P. Engels, and M. A. Hofer, Formation of dispersive shock waves by merging and splitting Bose-Einstein condensates, *Physical Review Letters* **101**, 170404 (2008).
- [18] M. E. Mossman, M. A. Hofer, K. Julien, P. G. Kevrekidis, and P. Engels, Dissipative shock waves generated by a quantum-mechanical piston, *Nature Communications* **9**, 10.1038/s41467-018-07147-4 (2018).
- [19] S. Mossman, S. I. Mistakidis, G. C. Katsimiga, A. Romero-Ros, G. Biondini, P. Schmelcher, P. Engels, and P. G. Kevrekidis, Nonlinear stage of modulational instability in repulsive two-component Bose-Einstein condensates 10.48550/arXiv.2412.17083 (2024).
- [20] W. G. Unruh, Experimental black-hole evaporation?, *Phys. Rev. Lett.* **46**, 1351 (1981).
- [21] U. Leonhardt, T. Kiss, and P. Ohberg, Intrinsic instability of sonic white holes 10.48550/arXiv.gr-qc/0211069 (2002).
- [22] C. Barceló, S. Liberati, and M. Visser, Towards the observation of Hawking Radiation in Bose-Einstein condensates, *International Journal of Modern Physics A* **18**, 3735 (2003).

- [23] C. Mayoral, A. Recati, A. Fabbri, R. Parentani, R. Balbinot, and I. Carusotto, Acoustic white holes in flowing atomic Bose-Einstein condensates, *New Journal of Physics* **13**, 025007 (2011).
- [24] R. Tsuda, S. Tomizawa, and R. Suzuki, Acoustic black and white holes of potential flow in a tube, *Physical Review D* **107**, 104020 (2023).
- [25] T. Torres, S. Patrick, A. Coutant, M. Richartz, E. W. Tedford, and S. Weinfurter, Rotational superradiant scattering in a vortex flow, *Nature Physics* **13**, 833 (2017).
- [26] B. Horstmann, R. Schützhold, B. Reznik, S. Fagnocchi, and J. Ignacio Cirac, Hawking radiation on an ion ring in the quantum regime, *New Journal of Physics* **13**, 045008 (2011).
- [27] O. Lahav, A. Itah, A. Blumkin, C. Gordon, S. Rinott, A. Zayats, and J. Steinhauer, Realization of a Sonic Black Hole Analog in a Bose-Einstein Condensate, *Physical Review Letters* **105**, 240401 (2010).
- [28] J. Steinhauer, Observation of quantum hawking radiation and its entanglement in an analogue black hole, *Nature Physics* **12**, 959 (2016).
- [29] J. R. Muñoz de Nova, K. Golubkov, V. I. Kolobov, and J. Steinhauer, Observation of thermal Hawking radiation and its temperature in an analogue black hole, *Nature* **569**, 688 (2019).
- [30] V. I. Kolobov, K. Golubkov, J. R. Muñoz de Nova, and J. Steinhauer, Observation of stationary spontaneous Hawking radiation and the time evolution of an analogue black hole, *Nature Physics* **17**, 362 (2021).
- [31] H. Tamura, S. Khlebnikov, C.-A. Chen, and C.-L. Hung, Observation of self-oscillating supersonic flow across an acoustic horizon in two dimensions [10.48550/arXiv.2304.10667](https://arxiv.org/abs/10.48550/arXiv.2304.10667) (2023).
- [32] P. G. Kevrekidis, D. J. Frantzeskakis, and R. Carretero-González, *The defocusing nonlinear Schrödinger equation: from dark solitons to vortices and vortex rings* (SIAM, 2015).
- [33] R. J. LeVeque, *Finite Volume Methods for Hyperbolic Problems* (Cambridge University Press, 2002).
- [34] M. R. Andrews, D. M. Stamper-Kurn, H.-J. Miesner, D. S. Durfee, C. G. Townsend, S. Inouye, and W. Ketterle, Propagation of sound in a Bose-Einstein condensate, *Phys. Rev. Lett.* **79**, 553 (1997).
- [35] M. R. Andrews, D. M. Stamper-Kurn, H.-J. Miesner, D. S. Durfee, C. G. Townsend, S. Inouye, and W. Ketterle, Erratum: Propagation of sound in a Bose-Einstein condensate [Phys. Rev. Lett. 79, 553 (1997)], *Physical Review Letters* **80**, 2967 (1998).
- [36] J. Steinhauer, R. Ozeri, N. Katz, and N. Davidson, Excitation spectrum of a Bose-Einstein condensate, *Physical Review Letters* **88**, 120407 (2002).
- [37] B. Demirkaya, T. Dereli, and K. Güven, Analog black holes and energy extraction by super-radiance from Bose-Einstein condensates (BEC) with constant density, *Heliyon* **5** (2019).
- [38] C. Mayoral, A. Recati, A. Fabbri, R. Parentani, R. Balbinot, and I. Carusotto, Acoustic white holes in flowing atomic Bose-Einstein condensates, *New Journal of Physics* **13**, 025007 (2011).
- [39] Y. Yang, Y. Wang, L. Zhao, D. Song, Q. Zhou, and W. Wang, Sonic black hole horizon formation for Bose-Einstein condensates with higher-order nonlinear effects, *AIP Advances* **9** (2019).
- [40] A. J. Hogg and E. W. G. Skevington, Dam-break reflection, *The Quarterly Journal of Mechanics and Applied Mathematics* **74**, 441 (2021).
- [41] M. Ungarish, A simple model for the reflection by a vertical barrier of a dam-break flow over a dry or pre-wetted bottom, *Journal of Fluid Mechanics* **942**, [10.1017/jfm.2022.338](https://doi.org/10.1017/jfm.2022.338) (2022).
- [42] C. Barceló, A. Cano, L. J. Garay, and G. Jannes, Stability analysis of sonic horizons in Bose-Einstein condensates, *Physical Review D* **74**, 024008 (2006).
- [43] R. Camassa, G. Falqui, G. Ortenzi, M. Pedroni, and G. Pitton, On the “vacuum” dam-break problem: Exact solutions and their long time asymptotics, *SIAM Journal on Applied Mathematics* **80**, 44 (2020).
- [44] J. Yang, Newton-conjugate-gradient methods for solitary wave computations, *Journal of Computational Physics* **228**, 7007 (2009).
- [45] J. Yang, *Nonlinear waves in integrable and nonintegrable systems* (SIAM, 2010).

## END MATTER

### Theoretical model and Computational methods

We describe the system using the 3D GP equation:

$$i\hbar \frac{\partial \Psi}{\partial t} = -\frac{\hbar^2}{2m} \nabla^2 \Psi + V(\mathbf{x})\Psi + g_{3d}|\Psi|^2\Psi, \quad (10)$$

where  $V(\mathbf{x}) = \frac{1}{2}m(\omega_x^2 x^2 + \omega_y^2 y^2 + \omega_z^2 z^2)$  is the external harmonic potential,  $m$  is the atomic mass of  $^{87}\text{Rb}$ , and  $g_{3d} = \frac{4\pi\hbar^2 a_s}{m}$  is the interatomic coupling coefficient determined by the scattering length  $a_s$ . The wavefunction  $\Psi(\mathbf{x}, t)$  is normalized such that the total number of atoms is  $\mathcal{N} = \int |\Psi|^2 d\mathbf{x}$ .

We perform numerical simulations of (10) for  $^{87}\text{Rb}$  atoms with a scattering length  $a_s = 100.4a_0$ , where  $a_0$  is the Bohr radius. The computational domain is a rectangular box with lengths  $\{L_x, L_y, L_z\} = \{1000, 5, 5\} \mu\text{m}$ , chosen to capture the elongated geometry of the system, discretized with  $\{N_x, N_y, N_z\} = \{2^{14}, 2^5, 2^5\}$  grid points. The ground state is computed using a Newton-conjugate-gradient method [44], initialized with a chemical potential of  $\mu = 135 \text{ nK}$  in the presence of a harmonic trap and a dam potential modeled by

$$V_d(\mathbf{x}) = U_d H(-X) \exp\left(-\frac{2X^2}{s_x^2} - \frac{2y^2}{s_y^2}\right) + U_d H(X), \quad (11)$$

with  $X = x - x_0$  where  $x_0$  represents the center of the dam and  $H(x)$  is the Heaviside step function. For best-fit with the experimental data presented in this Letter, we use a value of  $x_0 \approx 10 \mu\text{m}$ , which is within the error in the experiment. The values for the barrier height  $U_d$ , Gaussian waists  $\{s_x, s_y\}$  and harmonic trap frequencies are taken from the experiment.

Time evolution is performed in the presence of only the harmonic trap using a second-order pseudo-spectral split-step scheme [45], to which the ground state serves as the initial condition. A time step of  $\Delta t = 0.005 \text{ ms}$  is used for integration. The local density and flow velocity are recovered as  $n = |\Psi|^2$  and  $\mathbf{u} = \mathbf{j}/n$ , where  $\mathbf{j}$  is the current density given by

$$\mathbf{j}(\mathbf{x}, t) = \frac{\hbar}{2mi} (\Psi^* \nabla \Psi - \Psi \nabla \Psi^*). \quad (12)$$

The RIs are recovered from (see, e.g. Equation (3))

$$r_{\pm} = \frac{\mathbf{u} \cdot \hat{\mathbf{x}}}{2} \pm \sqrt{\frac{g_{1d} \langle n \rangle}{m}}, \quad (13)$$

where  $\mathbf{u} \cdot \hat{\mathbf{x}}$  is the component of the flow velocity along the axis of the BEC and the notation  $\langle \cdot \rangle = \int \cdot dy dz$  denotes an integrated cross-section.

### Negligible quantum pressure

The dimensional 3D GP equation (10) can be recast in nondimensional form using the rescaled coordinates

$$t' = \omega_z t, \quad \mathbf{x}' = \frac{\mathbf{x}}{\ell}, \quad \Psi' = \frac{\ell^{3/2}}{\sqrt{\mathcal{N}}} \Psi, \quad \ell = \left( \frac{4\pi\hbar^2 a_s \mathcal{N}}{m^2 \omega_z^2} \right)^{1/5}. \quad (14)$$

This yields the nondimensional GP equation

$$i\varepsilon \Psi_t = -\frac{\varepsilon^2}{2} \nabla^2 \Psi + \frac{1}{2} (\alpha_x x^2 + \alpha_y y^2 + \alpha_z z^2) \Psi + |\Psi|^2 \Psi, \quad (15)$$

where the primes have been dropped. Here,  $\alpha_j = (\omega_j/\omega_z)^2$  for  $j \in \{x, y, z\}$  quantify relative strengths of the harmonic confinement in each direction. The wavefunction is normalized such that  $\int |\Psi|^2 d\mathbf{x} = 1$ . The dimensionless parameter

$$\varepsilon = \left( \frac{\hbar}{m\omega_z (4\pi a_s \mathcal{N})^2} \right)^{1/5} \quad (16)$$

quantifies the relative strength of quantum pressure. For parameters from experiment, we find  $\varepsilon^2 = 9.15 \times 10^{-5} \ll 1$ ,  $\alpha_x = 9.52 \times 10^{-5} \ll 1$ ,  $\alpha_y = 0.94 \approx 1$  and  $\alpha_z = 1$ .

Rewriting Eq. (15) in hydrodynamic form via the Madelung transformation  $\Psi = \sqrt{n} e^{i\Phi}$ , where  $\mathbf{u} = \nabla \Phi$ , gives

$$\begin{aligned} n_t + \nabla \cdot (n\mathbf{u}) &= 0, \\ (n\mathbf{u})_t + \nabla \cdot (n\mathbf{u} \otimes \mathbf{u} + p_{\text{quantum}}) &= -\nabla p_{\text{hydro}} - n\nabla V, \end{aligned} \quad (17)$$

where the hydrodynamic and quantum pressures are given by

$$p_{\text{hydro}} = \frac{1}{2} n^2, \quad p_{\text{quantum}} = -\frac{\varepsilon^2}{4} n (\nabla \otimes \nabla) \log n. \quad (18)$$

This shows the quantum pressure, proportional to  $\varepsilon^2$ , away from sharp density transitions, is negligible compared to the hydrodynamic pressure, justifying its omission in the analysis.

### Interatomic coupling coefficient

Neglecting the quantum pressure, the interatomic coupling coefficient,  $g_{1d}$ , can be determined analytically using the (dimensional 1D) Thomas-Fermi (TF) density profile,

$$|\psi_{\text{TF}}| = \sqrt{\frac{\mu - V_h(x) - V_d(x)}{g_{1d}}}, \quad (19)$$

which is valid in the TF region defined by  $\mu > V_h(x) + V_d(x)$  and vanishes elsewhere. Here,  $V_h(x) = \frac{1}{2}m\omega_x^2 x^2$  and  $V_d(x) = U_d H(-x) \exp(-\frac{2x^2}{s_x^2}) + U_d H(x)$ . The normalization of the wavefunction is such that  $\int |\psi_{\text{TF}}|^2 dx = \mathcal{N}$ , yielding

$$g_{1d} = \frac{1}{\mathcal{N}} \int_{-R_{\text{TF}}}^{-\sqrt{2}s_x} [\mu - V_h(x) - V_d(x)] dx. \quad (20)$$

The upper bound in (20) is valid for  $ms_x^2\omega_x^2/U_d \ll 1$ . The lower bound is the TF radius

$$R_{\text{TF}} = \sqrt{\frac{2\mu}{m\omega_x^2}}. \quad (21)$$

Evaluating (20) for  $s_x \ll R_{\text{TF}}$  yields

$$g_{1d} = \frac{1}{\mathcal{N}} \left( \frac{2}{3}\mu R_{\text{TF}} - \sqrt{\frac{\pi}{2}}s_x U_d \text{erfc}(1) \right), \quad (22)$$

where  $\text{erfc}(x) = 1 - \text{erf}(x)$ . For the parameters from the experiments, Eq. (22) gives  $g_{1d} = 0.238$ . The exact value of  $g_{1d}$  from the integral in Eq. (20) is 0.223, showing that (22) is fairly accurate.

Equation (22) explicitly separates the interatomic coupling constant into two distinct contributions: the first term, proportional to  $R_{\text{TF}}$ , represents the idealized scenario of an infinitely sharp barrier, while the second term, proportional to the Gaussian waist  $s_x$ , introduces a negative correction arising from the finite width of the Gaussian potential. This correction quantifies how deviations from the idealized sharp-jump barrier influence the effective coupling constant.

#### Left edge of the rarefaction flow

We seek an explicit form for the left edge of the rarefaction flow. Numerical simulations of the 1D rarefaction dynamics, initialized with ground-state data, suggest that the left edge of the rarefaction flow reaches the left boundary of the BEC precisely when the right edge undergoes gradient catastrophe, at time  $T_{\text{gc}} = \frac{2\pi}{3\omega_x}$ . Guided by these observations and motivated by symmetry considerations, we assume the left edge shares the same functional form as the right edge in Eq. (7), leading to

$$x_l(t) = -\frac{\lambda_0 s_0}{\omega_x} \sin\left(\frac{\omega_x t}{\lambda_0}\right), \quad (23)$$

where  $\lambda_0$  is an undetermined positive parameter. This expression reduces to  $x_l(t) = -s_0 t$  in the limit  $\omega_x \rightarrow 0$ , recovering the known result in the absence of an external potential. To determine  $\lambda_0$ , we evaluate  $x_l(t)$  at  $t = T_{\text{gc}}$  and equate it to the TF radius. Using (21) and  $s_0 = \sqrt{\mu/m}$ , which is valid for a sharp jump in initial density, leads to the transcendental relation

$$\sin\left(\frac{2\pi}{3\lambda_0}\right) = \frac{\sqrt{2}}{\lambda_0}. \quad (24)$$

The unique root of this relation is

$$\lambda_0 = 1.4208602050622527\dots, \quad (25)$$

which is close to  $\sqrt{2}$ , with a relative error of 0.47%. For convenience, we approximate this value by  $\sqrt{2}$ , yielding (8).

#### Matched solution

Suppressing explicit time dependence for clarity, the coefficients appearing in Eq. (9) are given by:

$$\begin{aligned} c_0 &= -(\alpha - c_2 x_r)x_r, & u_0 &= v_r - (\beta - u_2 x_r)x_r, \\ c_1 &= \alpha - 2c_2 x_r, & u_1 &= \beta - 2u_2 x_r, \\ c_2 &= \frac{\alpha}{x_r - x_l} + \frac{C_l}{(x_r - x_l)^2}, & u_2 &= \frac{\beta}{x_r - x_l} - \frac{v_r}{(x_r - x_l)^2}, \end{aligned} \quad (26)$$

with

$$v_r(t) = \frac{dx_r}{dt} = 2s_0 \cos(\omega_x t), \quad C_l(t) = \sqrt{\frac{g_{1d}}{m}} |\psi_{\text{TF}}(x_l(t))|.$$

Here,  $|\psi_{\text{TF}}(x)|$  is the Thomas-Fermi density profile given by Eq. (19), and  $x_l(t)$  is the left edge defined in Eq. (8). The time-dependent coefficients  $\alpha(t)$  and  $\beta(t)$  are given by:

$$\alpha(t) = -\frac{\omega_x}{2} \csc\left(\frac{3\omega_x t}{2}\right), \quad \beta(t) = \omega_x \cot\left(\frac{3\omega_x t}{2}\right).$$

Since the matched solution is quadratic in space, we do not expect it to accurately describe the dynamics close to the gradient catastrophe time. When compared to numerical simulations, the matched solution demonstrates excellent agreement for times below 100 ms but exhibits significant deviations near the gradient catastrophe time  $T_{\text{gc}} \approx 136$  ms.